



## 저작자표시-비영리-변경금지 2.0 대한민국

이용자는 아래의 조건을 따르는 경우에 한하여 자유롭게

- 이 저작물을 복제, 배포, 전송, 전시, 공연 및 방송할 수 있습니다.

다음과 같은 조건을 따라야 합니다:



저작자표시. 귀하는 원저작자를 표시하여야 합니다.



비영리. 귀하는 이 저작물을 영리 목적으로 이용할 수 없습니다.



변경금지. 귀하는 이 저작물을 개작, 변형 또는 가공할 수 없습니다.

- 귀하는, 이 저작물의 재이용이나 배포의 경우, 이 저작물에 적용된 이용허락조건을 명확하게 나타내어야 합니다.
- 저작권자로부터 별도의 허가를 받으면 이러한 조건들은 적용되지 않습니다.

저작권법에 따른 이용자의 권리는 위의 내용에 의하여 영향을 받지 않습니다.

이것은 [이용허락규약\(Legal Code\)](#)을 이해하기 쉽게 요약한 것입니다.

[Disclaimer](#)

공학석사 학위논문

# Cation Exchange Strategy for Fabrication of CsPbBr<sub>3</sub> Perovskite Solar Cell

CsPbBr<sub>3</sub> 페로브스카이트 태양전지 제조를 위한  
양이온 교환 전략

2023년 8월

서울대학교 대학원

재료공학부

박진호

# Cation Exchange Strategy for Fabrication of CsPbBr<sub>3</sub> Perovskite Solar Cell

지도교수 김 진 영

이 논문을 공학석사 학위논문으로 제출함  
2023년 8월

서울대학교 대학원  
재료공학부  
박 진 호

박진호의 공학석사 학위논문을 인준함  
2023년 8월

위 원 장 \_\_\_\_\_ 장 호 원 (인)

부위원장 \_\_\_\_\_ 김 진 영 (인)

위 원 \_\_\_\_\_ 권 민 상 (인)

# Abstract

## **Cation Exchange Strategy for Fabrication of CsPbBr<sub>3</sub> Perovskite Solar Cell**

Jinho Park

Department of Materials Science and Engineering

The Graduate school

Seoul National University

All-inorganic CsPbBr<sub>3</sub> perovskite solar cell is attracting attention due to its high voltage output and negligible level of stability against humidity and temperature compared to organic-inorganic perovskite solar cells. However, the limited solubility of CsBr remains an obstacle for the production of CsPbBr<sub>3</sub> films intended for use in perovskite solar cells. In this study, we present a cation exchange strategy for the synthesis of all-inorganic CsPbBr<sub>3</sub> films. By exploiting the high solubility of CsAc (Cesium Acetate) in methanol, we have achieved the

conversion of the organic  $\text{DMA}_{0.3}\text{MA}_{0.7}\text{PbBr}_3$  film (DMA = Dimethylammonium cation, MA = Methylammonium cation) to an all-inorganic  $\text{CsPbBr}_3$  film by facile two-step spin coating. Therefore, a high-quality  $\text{CsPbBr}_3$  film featuring a uniform, flat, sizable grain structure, and minimal secondary phase was successfully produced. The material property of the as made  $\text{CsPbBr}_3$  film is studied. And its formation mechanism is proposed. Moreover, as an application, a perovskite solar cell is realized using the  $\text{CsPbBr}_3$  film, demonstrating an efficiency as high as 5.9% with remarkably high  $V_{\text{oc}}$  (1.4 V).

**Keywords:**  $\text{CsPbBr}_3$ , Solubility, Solar cell, Perovskite, Two-step method, Cesium acetate.

**Student Number:** 2021-27260

# Table of Contents

<b>Abstract .....</b>	<b>i</b>
<b>Table of Contents .....</b>	<b>iii</b>
<b>List of Tables .....</b>	<b>v</b>
<b>List of Figures .....</b>	<b>vi</b>
<b>Chapter 1. Introduction .....</b>	<b>1</b>
1.1 Recent Researches and Developments in Perovskite solar cells.....	1
1.2 Properties and fabricating issues of CsPbBr <sub>3</sub> perovskite structure .....	2
1.3 Cation exchange strategy for fabricating CsPbBr <sub>3</sub> perovskite solar cell.....	3
<b>Chapter 2. Background.....</b>	<b>7</b>
2.1 The properties of CsPbBr <sub>3</sub> material .....	7
2.2 The processing issue of CsPbBr <sub>3</sub> solar cell .....	8
<b>Chapter 3. Experimental Details.....</b>	<b>12</b>
3.1 Materials .....	12
3.2 Fabrication of CsPbBr <sub>3</sub> films .....	13
3.3 Fabrication of Solar Cells .....	13
3.4 Characterization .....	14

<b>Chapter 4. Results and Discussion.....</b>	<b>15</b>
4.1 Mechanism of CsPbBr <sub>3</sub> film fabrication.....	15
4.2 Material analyzation of CsPbBr <sub>3</sub> film .....	27
4.3 Optical properties of CsPbBr <sub>3</sub> film .....	38
4.4 Device characterization .....	45
<b>Chapter 5. Conclusion.....</b>	<b>49</b>
<b>Bibliography.....</b>	<b>50</b>
<b>Abstract in Korean.....</b>	<b>58</b>

## List of Tables

<b>Table 4.1.1.</b> Mass spectroscopy data which shows type of gas collected at 200 °C .....	26
<b>Table 4.2.1.</b> Calculation of the composition ratio of film through the area of the NMR spectrum corresponding to the MA <sup>+</sup> peak and the DMA <sup>+</sup> peak of the DMA <sub>0.3</sub> MA <sub>0.7</sub> PbBr <sub>3</sub> film.....	37
<b>Table 4.3.1.</b> Time resolved photoluminescence (TRPL) characterization of the CsPbBr <sub>3</sub> perovskite film on glass and SnO <sub>2</sub> layer.....	44
<b>Table 4.4.1.</b> Stability data of the PSC after storing in N <sub>2</sub> atmosphere (with a temperature of ~25 °C) over 120 days without any encapsulation. ....	48



# List of Figures

<b>Figure 1.1.1.</b> A graph illustrating the certified efficiencies of different cells spanning from 1975 to the present [1] .....	5
<b>Figure 1.2.1.</b> Various fabrication methods for CsPbBr <sub>3</sub> solar cell.....	6
<b>Figure 2.1.1.</b> Simulated crystal structure of cubic CsPbBr <sub>3</sub> [2] .....	10
<b>Figure 2.2.1.</b> Three-dimensional crystal models of CsPb <sub>2</sub> Br <sub>5</sub> , CsPbBr <sub>3</sub> , and Cs <sub>4</sub> PbBr <sub>6</sub> structures. Reprinted with permission from [3]. Copyright 2019 American Chemical Society. ....	11
<b>Figure 4.1.1.</b> Image of (a) CsBr powders and CsAc powders in vials (b) CsBr powders in 1ml mixture of methanol solvents at 25 °C (0.05 M~0.1 M) and CsAc powders in 1ml mixture of methanol solvents at 25 °C (2.0 M). (c) Large size photograph of CsBr powders in 1ml mixture of methanol solvents (0.1 M) at 25 °C .....	20
<b>Figure 4.1.2.</b> Scheme of mechanism about CsPbBr <sub>3</sub> film fabrication .....	21
<b>Figure 4.1.3.</b> TGA curve of CsAc+DMA <sub>0.3</sub> MA <sub>0.7</sub> PbBr <sub>3</sub> film before annealing...	22
<b>Figure 4.1.4.</b> NMR spectra of DMA <sub>0.3</sub> MA <sub>0.7</sub> PbBr <sub>3</sub> film and as-treated film.....	23
<b>Figure 4.1.5.</b> XRD curves of CsPbBr <sub>3</sub> films with increasing annealing time at 225 °C .....	24
<b>Figure 4.1.6.</b> XRD curves of CsPbBr <sub>3</sub> films with increasing concentration of CsAc at 225 °C .....	25
<b>Figure 4.2.1.</b> NMR spectra of DMA <sub>0.3</sub> MA <sub>0.7</sub> PbBr <sub>3</sub> film and CsPbBr <sub>3</sub> film.....	30

<b>Figure 4.2.2.</b> XPS curves (N 1s) of DMA <sub>0.3</sub> MA <sub>0.7</sub> PbBr <sub>3</sub> film and CsPbBr <sub>3</sub> film	31
<b>Figure 4.2.3.</b> XPS curves ((a) Cs 3d, (b) Pb 4f, (c) Br 3d) of CsPbBr <sub>3</sub> film	32
<b>Figure 4.2.4.</b> SEM images ((a) top view of DMA <sub>0.3</sub> MA <sub>0.7</sub> PbBr <sub>3</sub> film and (b) CsPbBr <sub>3</sub> film) and photograph of each film.	33
<b>Figure 4.2.5.</b> Histograms of the diameters (denoted as grain sizes) and the area of CsPbBr <sub>3</sub> perovskite grains measured by Image J	34
<b>Figure 4.2.6.</b> SEM images ((a) cross view of DMA <sub>0.3</sub> MA <sub>0.7</sub> PbBr <sub>3</sub> film and (b) CsPbBr <sub>3</sub> film)	35
<b>Figure 4.2.7.</b> XRD curve of pure CsPbBr <sub>3</sub> film with non-secondary phase	36
<b>Figure 4.3.1.</b> UV-Vis spectra of DMA <sub>0.3</sub> MA <sub>0.7</sub> PbBr <sub>3</sub> film and CsPbBr <sub>3</sub> film	40
<b>Figure 4.3.2.</b> Tauc plot of DMA <sub>0.3</sub> MA <sub>0.7</sub> PbBr <sub>3</sub> film and CsPbBr <sub>3</sub> film from UV-Vis spectra	41
<b>Figure 4.3.3.</b> Steady-state PL spectra of CsPbBr <sub>3</sub> /glass film	42
<b>Figure 4.3.4.</b> TRPL spectra of CsPbBr <sub>3</sub> film with each layer (glass, SnO <sub>2</sub> )	43
<b>Figure 4.4.1.</b> <i>J-V</i> curve of CsPbBr <sub>3</sub> perovskite solar cell and photovoltaic parameters	46
<b>Figure 4.4.2.</b> EQE analysis of CsPbBr <sub>3</sub> perovskite solar cell	47

# Chapter 1. Introduction

## **1.1. Recent Researches and Developments in Perovskite solar cells**

Global efforts such as the Parties to the 2015 Paris Agreement are being urged to limit the increase in temperature up to 1.5 °C compared to the era of the industrial revolution.[4] Fossil fuels are known to be the main cause of global warming due to greenhouse gases generated during combustion, and have various problems such as limited reserves,[5] and air pollution.[6]

To solve this problem, photovoltaics has attracted great interest. Perovskite Solar Cells (PSCs) have the advantages of being able to be processed at a low temperature with cheap materials. In addition, PSC has advantages such as easily tunable bandgap,[7, 8] low exciton binding energy,[9] high carrier mobility,[10] and high absorption coefficient, attracting attention as a next-generation solar cell. With this explosive interest, PSCs have brought rapid developments in performances with the power conversion efficiency (PCE) from the initial 3.8% to 25.73% certified PCE [11] on single junction perovskite devices as shown in Figure 1.1.1. which is now on par with the state-of-the-art Si solar cell efficiency (26.8%).[1] Moreover, along with the development of perovskite solar cell, perovskite/Si tandem solar cell technology to overcome Shockley-Queisser limit of

single junction solar cell (33.77%) has rapidly advanced with the record PCE of 32.5%. [1, 12]

However, organic-inorganic hybrid solar cells (PSCs) are vulnerable to various environmental stimuli due to the fundamental limitations of composition.[13, 14] High humidity promotes the production of halide salt ( $\text{PbI}_2$ ) by causing the degradation of perovskite structure.[15] In addition, continuous temperature rise due to sun illumination causes phase change and instability of perovskite layer.[16]

## **1.2. Properties and fabricating issues of $\text{CsPbBr}_3$ perovskite structure**

The all-inorganic ( $\text{CsPbX}_3$ ) perovskites structure has a negligible level of stability against environmental factors and has begun to attract increasing attention as a photovoltaic material.[17, 18] Among them,  $\text{CsPbBr}_3$  perovskite structure has a bandgap of about 2.3 eV,[19] maintaining higher phase stability [20] than  $\text{CsPbI}_3$  perovskite structure, and has a lower bandgap than  $\text{CsPbCl}_3$  (~3.0 eV),[21] so it is suitable for use in the photoactive layer. In addition, it can theoretically generate a high voltage output of about 2.0 V, so it can be utilized in various ways such as LEDs and catalysts other than solar cells.[22, 23]

However, the low solubility of CsBr made it difficult to form enough thickness to use  $\text{CsPbBr}_3$  as a photoactive layer and an obstacle to making reproducible thin films in solution-processed methods.[3, 24] So far, various solution-processed methods have been proposed as shown in Figure 1.2.1. First, the dipping method produces a Cs-Pb-Br film by exposing a solution dissolved in CsBr to a film

obtained by deposited  $\text{PbBr}_2$  for a long time. However, this requires a long and appropriate dipping time, and mixed phase appears in the film, leading to pore morphology.[25-27] The multi-step spin coating method has advantages of more easily suppressing the secondary phase because it dissolves CsBr in methanol, spin coating several times, and repeats annealing to form Cs-Pb-Br film.[28, 29] However, this is time-consuming and has the disadvantage of reducing reproducibility due to a large number of spin coatings.[3, 30] In order to reduce the number of coatings required for CsBr deposition, a solvent with high solubility for CsBr was employed.[31, 32] A two-step spin coating method has been proposed, but there is still an inconvenience of pre-heating the  $\text{PbBr}_2$  substrate about 70 °C to obtain good crystallinity, and the morphology changes greatly depending on the loading time of the solvent.[33]

### **1.3. Cation exchange strategy for fabricating $\text{CsPbBr}_3$ perovskite solar cell.**

In this study, We propose a novel two-step spin coating-based Cs-Pb-Br film fabrication method that can solve the solubility problem and enhance reproducibility. Until recently, a process of dissolving a small amount of CsBr in methanol and spin-coating (0.07 M) at  $\text{PbBr}_2$  layer several times was mainly used. In contrast, CsAc has been newly discovered to be a Cs source that dissolves very well in methanol. Using this, we present a cation exchange strategy for the synthesis of all-inorganic  $\text{CsPbBr}_3$  films. We employ spin-coating to deposit a CsAc/methanol solution onto a DMA-MA- $\text{PbBr}_3$  film, followed by a cation

exchange reaction to convert the organic cation to  $\text{Cs}^+$ . This film exhibits a minimal amount of secondary phase and a relatively large grain size, which is accompanied by a low occurrence of pinholes. Furthermore, the proposed method is advantageous in terms of reproducibility as it removes the need for  $\text{PbBr}_2$  substrate preheating, which is required in existing original multi-step and two-step spin coating techniques.



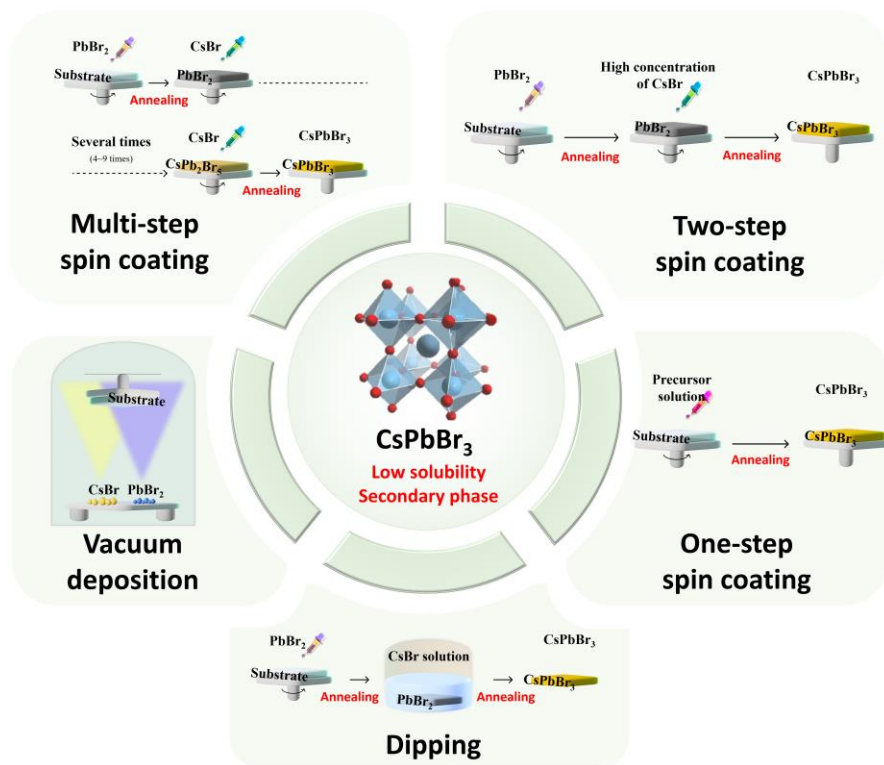


**Figure 1.2.1.** Various fabrication methods for  $\text{CsPbBr}_3$  solar cell



## Chapter 2. Background

### 2.1. The properties of CsPbBr<sub>3</sub> material

Figure 2.1.1 shows crystal structure of cubic CsPbBr<sub>3</sub>. The CsPbBr<sub>3</sub> material demonstrates superior thermal and moisture stability when compared to other perovskite structures, as supported by research studies.[17, 18] Specifically, this material exhibits minimal degradation when exposed to high temperatures, with a thermal stability threshold of 416 °C.[34] Furthermore, the performance of CsPbBr<sub>3</sub>-based solar cells remains relatively unaffected even after being subjected to high humidity environments for extended periods, as evidenced by studies lasting several hundred hours.[3, 22] This can be attributed to its appropriate tolerance factor (0.862) which allows it to thermodynamically form a cubic phase, as well as its more negative value of enthalpy of formation ( $-11.64 \pm 1.17$  kJ/mol) compared to other perovskite structures.[35] Additionally, the use of an inorganic cation (Cs) rather than an organic cation (such as Formamidinium (FA) or Methylammonium (MA)) contributes to its superior thermal and hygroscopic stability.[36] Notably, the fact that CsPbBr<sub>3</sub> consists of a single halide composition means that halide aggregation does not occur, which further enhances its stability.

At room temperature, the bulk form of CsPbBr<sub>3</sub> adopts an orthorhombic structure,

but upon heating, it undergoes a structural transition to a tetragonal phase at 88 °C and to a cubic phase at 130 °C.[37] Despite these structural changes, each phase exhibits similar optical and electrical properties, rendering CsPbBr<sub>3</sub> a promising photoactive material that can maintain its functionality over an extended duration, even under ambient conditions.[38]

The suitability of CsPbBr<sub>3</sub> as a photoactive material stems from its high electron mobility (1000 cm<sup>2</sup>/(V·s)), long lifetime (2.5 μs),[38] and wide range of observable optical properties.[39, 40] Its bandgap of 2.3 eV allows for a theoretical high voltage output of 2.0 V, making it a potential candidate for use in multi-junction tandem solar cells, LEDs, and PV-EC applications.[22, 23, 41]

## **2.2. The processing issue of CsPbBr<sub>3</sub> solar cell**

The manufacturing of CsPbBr<sub>3</sub> perovskite solar cells faces two significant challenges. Firstly, due to the low solubility of precursor materials in the solvent, it is challenging to form perovskite into a film through the solution process. This limitation is particularly evident in the one-step spin-coating method, which is commonly used to form the organic-inorganic perovskite photoactive layer. This is because CsBr has low solubility in the solvent, and there is a large solubility difference between CsBr and PbBr<sub>2</sub>. Although CsBr can be dissolved in a DMSO/DMF solvent up to 0.4 M to 0.5 M.[42] the resulting deposition thickness is approximately 200 nm, which is insufficient for the photoactive layer in a solar cell. Researchers are exploring various strategies to overcome this limitation, such as multistep spin-coating methods,[23] selective solvents that dissolve CsBr,[43, 44]

or using other precursors that provide Cs.[45, 46]

The second challenge is to control the occurrence of the secondary phase. Depending on the atomic ratio of Cs, Pb, and Br, the Cs-rich ( $\text{Cs}_4\text{PbBr}_6$ ) phase and Pb-rich ( $\text{CsPb}_2\text{Br}_5$ ) phase are easily formed as illustrated in Figure 2.2.1. These phases have a high bandgap ( $> 3.2$  eV) [47, 48] and lower the photoelectric efficiency of the solar cell device.[49, 50] Therefore, it is critical to form a pure  $\text{CsPbBr}_3$  phase with the appropriate stoichiometry. Various approaches have been proposed to overcome this challenge, such as suppressing the generation of secondary phase by calculating the generated energy of each phase [51] or using a solvent such as EGME to suppress the secondary phase.[32, 52] Additionally, halide substitution can be used to fix the amounts of Cs and Pb and form  $\text{CsPbBr}_3$  with little secondary phase.[53]

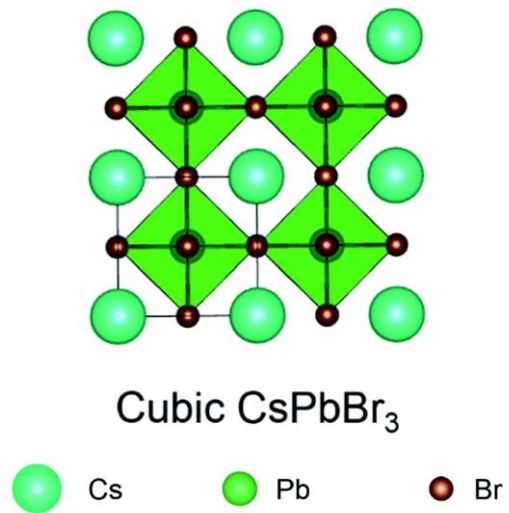


**Figure 2.1.1.** Simulated crystal structure of cubic CsPbBr<sub>3</sub> [2]

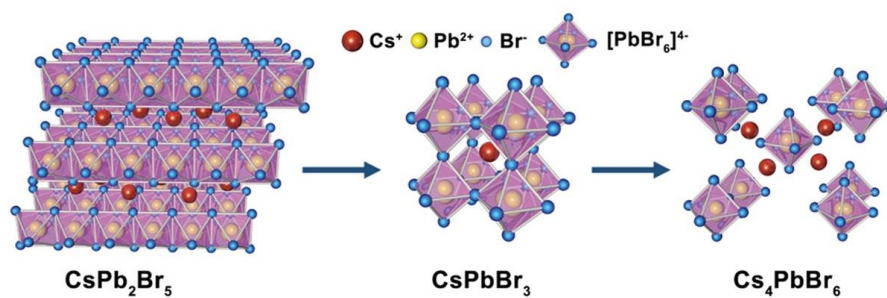


**Figure 2.2.1.** Three-dimensional crystal models of  $\text{CsPb}_2\text{Br}_5$ ,  $\text{CsPbBr}_3$ , and  $\text{Cs}_4\text{PbBr}_6$  structures. Reprinted with permission from [3]. Copyright 2019 American Chemical Society

## Chapter 3. Experimental Details

### 3.1 Materials

Methylammonium bromide (MABr) (>99.99%), Dimethylammonium bromide(DMABr) were purchased from Greatcell Solar Materials. Lead Bromide ( $\text{PbBr}_2$ ) (99.999%),  $\text{SnO}_2$  colloid precursor [tin(IV) oxide, 15% in  $\text{H}_2\text{O}$  colloidal dispersion] was purchased from Alfa Aesar. Cesium Acetate ( $\text{CsAc}$ ) ( $\geq 99.99\%$ ), Dimethyl sulfoxide (DMSO, anhydrous,  $\geq 99.9\%$ ), N,N-Dimethylformamide (DMF, anhydrous,  $\geq 99.8\%$ ), Methanol (anhydrous, 99.8%), Nickel(II) acetate tetrahydrate ( $\geq 99.0\%$ ), tBP, chlorobenzene, acetonitrile, LiTFSI were purchased from Sigma Aldrich.  $\text{C}_{60}$  was purchased from nano-c. Ethanol (Anhydrous, 99.9%) was purchased from OCI. spiro-MeOTAD was purchased from Lumtec.

### 3.2 Fabrication of CsPbBr<sub>3</sub> films

2.0 M of perovskite precursor solution was prepared by dissolving DMABr, MABr, and PbBr<sub>2</sub> (DMA<sub>0.3</sub>MA<sub>0.7</sub>PbBr<sub>3</sub>) in DMF and DMSO (DMF:DMSO = 1:1; volume ratio). 1.0 M of solution was prepared by dissolving CsAc in Methanol. To fabricate CsPbBr<sub>3</sub> perovskite films, two step spin coating method was used. Precursor solution was spin-coated on substrates at 3,000 rpm for 30 s. 1mL of Ethyl ether was dripped on wet films at 25 s after start of spinning. After spinning, films were annealed at 100°C for 3 min. Then, CsAc solution was spin coated on these films at 4000 rpm for 20 s, followed by 225°C treatment for 30min.

### 3.3 Fabrication of Solar Cells

ITO's were successively cleaned with detergent, deionized water, IPA, and UV–ozone treatment. For preparing SnO<sub>2</sub> electron transport layers, SnO<sub>2</sub> colloid precursor solution was used. The solution was spin-coated on ITO substrates at 3000 rpm for 30 s and then baked on a hot plate in ambient air at 150°C for 30 min. Next, perovskite films are spin-coated by the above-mentioned method. And then, the classic spiro-MeOTAD precursor solution was prepared by dissolving 70 mg spiro-OMeTAD, 28 µl tBP and 20.4 µl lithium bis(trifluoromethanesulfonyl)imide solution (520 mg/cc in acetonitrile) in 1 cc of chlorobenzene. The spiro-MeOTAD solution was spin-coated on top of the perovskite films at 3000 rpm for 30 s. Then,

120 nm-thick Au layer was deposited on top of the films layer by thermal evaporation.

### 3.4 Characterization

Structural analysis of films were investigated by XRD with Cu K $\alpha$  radiation (XRD; New D8 Advance, Bruker). Optical properties of films were measured by UV-vis spectroscopy (Cary5000, Agilent). The top-view and cross-sectional images of films and devices were examined by SEM (JSM-7600F, JEOL). PL, TRPL datas were investigated by measuring PL spectrum periodically at room temperature under ambient atmosphere condition with continuous 405 nm laser illumination (FlouTime 300, PicoQuant). J-V measurement of single-junction solar cells were conducted with potentiostat under AM 1.5G illumination (100 mW/cm<sup>2</sup>) by solar simulator (potentiostat; CHI 608C, CH Instruments, solar simulator; PEC-L11, Pecell Technologies, AAA graded). The J-V measurements were conducted with aperture whose size is 0.14 cm<sup>2</sup> by metal mask for single-junction devices. The scan rates of J-V were 240 mV/s for single-junction devices. The J-V scans were conducted in ambient atmosphere at room temperature without any preconditioning such as light soaking. Composition of crystals was investigated by H-NMR (AVANCE 600, Bruker). Solutions for H-NMR were prepared by dissolving precipitated powder in DMSO-d<sub>6</sub> (JeolJNM-LA400, JEOL). For investigation of residue NH<sub>3</sub><sup>+</sup> cations and change in the binding energy of the composition in perovskite films, XPS was conducted (AXIS SUPRA, Kratos). To observe the components of the gas generated when cation exchange reaction occurs, TGA-



GC/MS was conducted (TGA : pyris 1, GC:clarus 680, MS:clarus SQ8T).

## Chapter 4. Results and Discussion

### 4.1 Mechanism of CsPbBr<sub>3</sub> film fabrication

Previously, studies on producing high-quality perovskite structure using acetate such as lead acetate and ethyl acetate have been actively conducted.[54-56] This is because acetates have very good solubility in polar events such as DMSO, DMF, and methanol. CsAc also has high solubility in polar solvents such as methanol. This became the main background for using CsAc (>2.0 M) as the new precursor for CsPbBr<sub>3</sub> instead of CsBr with low solubility (0.07 M).[45]

To determine the solubility of each powder of CsBr and CsAc for methanol, we conducted a solubility experiment. A certain amount of CsBr powders and CsAc powders were added to each vial, and 1 ml methanol was then mixed. **Figure 4.1.1** shows that CsBr was dissolved in methanol up to 0.07M, but not completely dissolved at higher concentrations. On the other hand, CsAc powders, which correspond to 2.0 M concentration, were all dissolved in methanol. This can prove that CsAc has much higher solubility in methanol than CsBr.

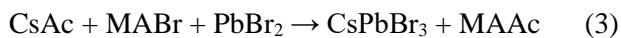
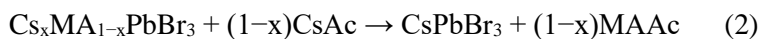
As shown in **Figure.4.1.2**, CsPbBr<sub>3</sub> in this work is prepared by two step approach

by spin coating. First,  $\text{DMA}_{0.3}\text{MA}_{0.7}\text{PbBr}_3$  precursor is one step spin-coated on the substrates to manufacture base films. After soft annealing, these are spin-coated with CsAc dissolved in methanol at an appropriate concentration. Finally, a pure and uniform  $\text{CsPbBr}_3$  film is formed through an annealing process in ambient condition.

It has been previously reported that the mechanism for making  $\text{CsPbBr}_3$  using CsAc is carried out through eqn.1 as follows [46].



In a state in which annealing is not performed in the above reaction, it is considered that the MAAc components remains in the  $\text{Cs}_x\text{MA}_{1-x}\text{PbBr}_3$  grains without volatilization due to Pb-Ac bond. Through the high-temperature annealing process, the remaining MA cations are finally replaced with Cs cations to form  $\text{CsPbBr}_3$ .



However, through additional measurement and analysis, it was confirmed that the reaction was somewhat different from the above mechanism. We scraped powder from CsAc-treated  $\text{DMA}_{0.3}\text{MA}_{0.7}\text{PbBr}_3$  film and measured it with Thermogravimetric Analysis – mass spectroscopy (TGA-MS). The type of

molecules generated in the film during the heating process and the temperature at which the reaction takes place were identified. **Figure 4.1.3** shows that the mass of powder is mostly reduced from 100 °C to 200 °C. The results of analyzing the mass chromatogram of the collected gas components are also specified in **Table.4.1.1**. In most of the collected gases, organic molecules such as acetic acid, guanidine, and isopropylamine were observed. In addition, no peak was found for Cs, Pb, and Br. The mass reduction between 50 °C and 100 °C is estimated to be the evaporation of water[57] and methanol, and no mass reduction was observed at temperatures above 200°C. Therefore, it could be inferred that only the organic molecules were evaporated at a temperature within 200 °C. Furthermore, during annealing, it was found that organic molecules were not volatilized in the form of MA, DMA, or acetate, but were volatilized in the form of other organic molecules.

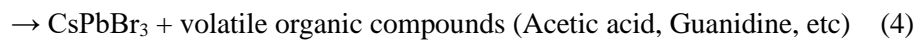
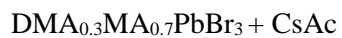
However, the TGA showed a mass loss of about 6 percent. This was less than the expected mass loss of about 15 percent when all organic components were volatilized. Therefore, it was assumed that some organic components were removed before the annealing process. To further investigate this, we performed NMR (**Figure 4.1.4**). The upper peak is from the  $\text{DMA}_{0.3}\text{MA}_{0.7}\text{PbBr}_3$  film, and the lower peak is from the film without going through the annealing process after processing CsAc. Only CsAc was treated, and it was confirmed that the peak representing organic components was significantly reduced compared to the reference peak. It is believed that certain organic components might have been dissolved by methanol during the CsAc treatment. Alternatively, it is possible that organic components interacted with acetate ions, leading to a transformation into a

volatile substance that subsequently evaporated as a film.

To observe changes in the crystal structure of organic  $\text{DMA}_{0.3}\text{MA}_{0.7}\text{PbBr}_3$  film to  $\text{CsPbBr}_3$  film over annealing time, we performed XRD analysis as shown in **Figure 4.1.5**. We detected the perovskite main peak of  $\text{DMA}_{0.3}\text{MA}_{0.7}\text{PbBr}_3$  film at approximately  $14.96^\circ$ , which is assumed to the (100) plane of perovskite structure. After treating the film with the appropriate concentration of CsAc, we observed a shift in the main peak towards higher angle as increasing annealing time, eventually reaching  $15.36^\circ$  after 30 minutes. This is almost consistent with the (100) plane of the  $\text{CsPbBr}_3$  crystal structure previously reported.[43] This results indicates that the organic component is almost volatilized, and  $\text{CsPbBr}_3$  structure is formed through appropriate annealing time.

**Figure 4.1.6** shows normalized XRD curves of  $\text{DMA}_{0.3}\text{MA}_{0.7}\text{PbBr}_3$  film and CsAc & heat treated perovskite films. In the film treated with a sufficient concentration of CsAc (0.9 M), the main peaks of perovskite dominantly appeared at  $15.3^\circ$ ,  $21.2^\circ$ , and  $30.8^\circ$  respectively, which are exactly consistent with the peaks of  $\text{CsPbBr}_3$ .[43] However, for the  $\text{CsPbBr}_3$  film prepared from a low concentration of CsAc, peak dominantly appeared at  $11.7^\circ$  which corresponds to the (110) plane of the Pb-rich phase of  $\text{CsPb}_2\text{Br}_5$  [43]. On the other hand, when the concentration of CsAc is greater than the appropriate concentration, new peaks dominantly appeared at  $12.71^\circ$  and  $12.97^\circ$  which means Pb-deficit phase of  $\text{Cs}_4\text{PbBr}_6$  is formed.[43] These results confirm that the  $\text{DMA}_{0.3}\text{MA}_{0.7}\text{PbBr}_3$  film can be well transformed to  $\text{CsPbBr}_3$  film through the above-stated mechanism with a moderate CsAc concentration.

By applying these mechanisms, the principle of transforming  $\text{DMA}_{0.3}\text{MA}_{0.7}\text{PbBr}_3$  to  $\text{CsPbBr}_3$  can be inferred as eqn.4 in this study.



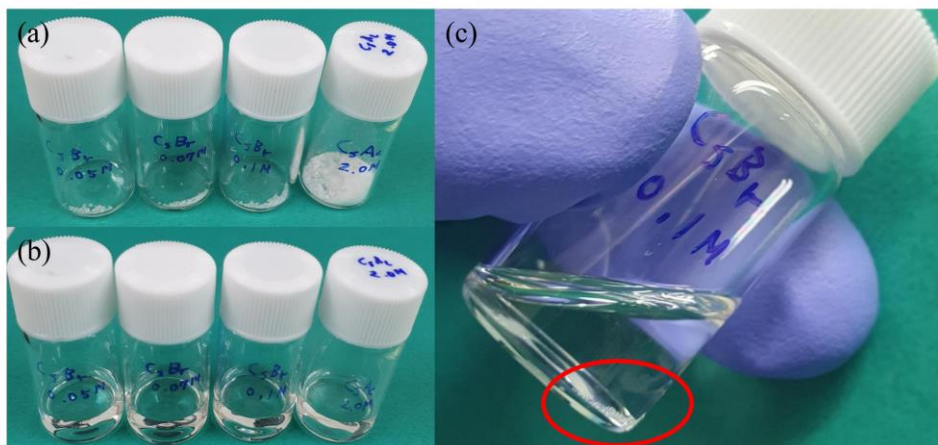


**Figure 4.1.1.** Image of (a) CsBr powders and CsAc powders in vials (b) CsBr powders in 1ml mixture of methanol solvents at 25 °C (0.05 M~0.1 M) and CsAc powders in 1ml mixture of methanol solvents at 25 °C (2.0 M). (c) Large size photograph of CsBr powders in 1ml mixture of methanol solvents (0.1 M) at 25 °C

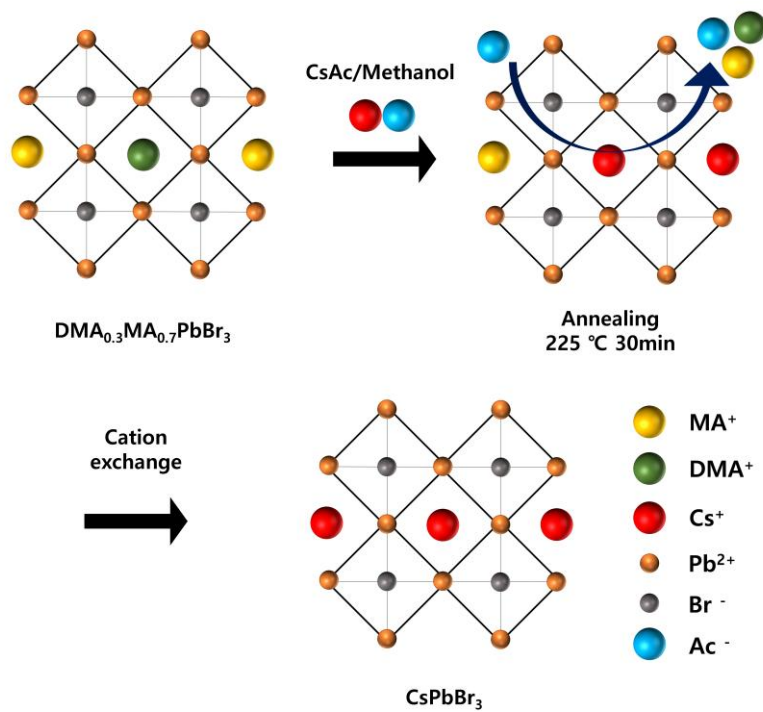


**Figure 4.1.2.** Scheme of mechanism about  $\text{CsPbBr}_3$  film fabrication

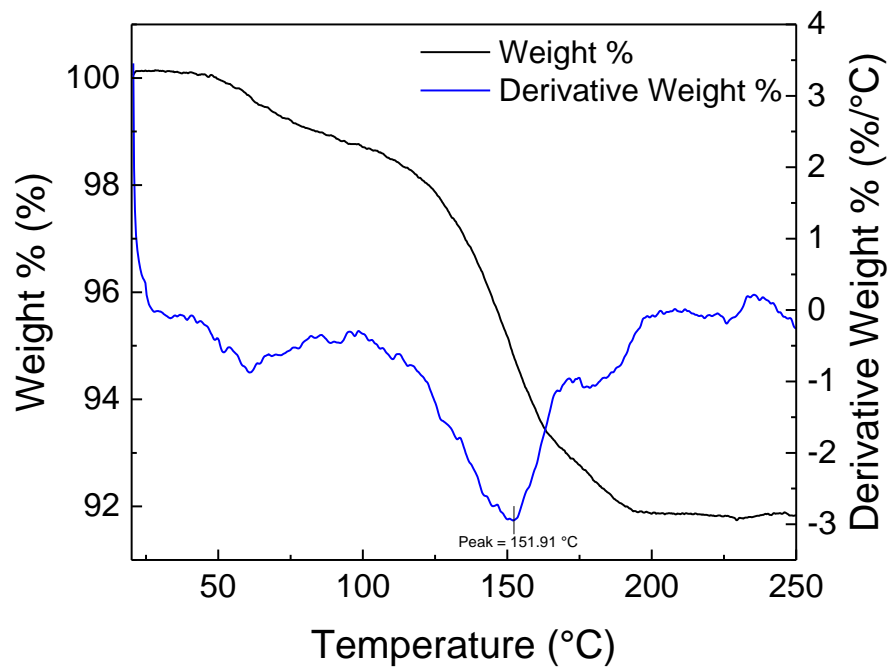


**Figure 4.1.3.** TGA curve of CsAc+DMA<sub>0.3</sub>MA<sub>0.7</sub>PbBr<sub>3</sub> film before annealing



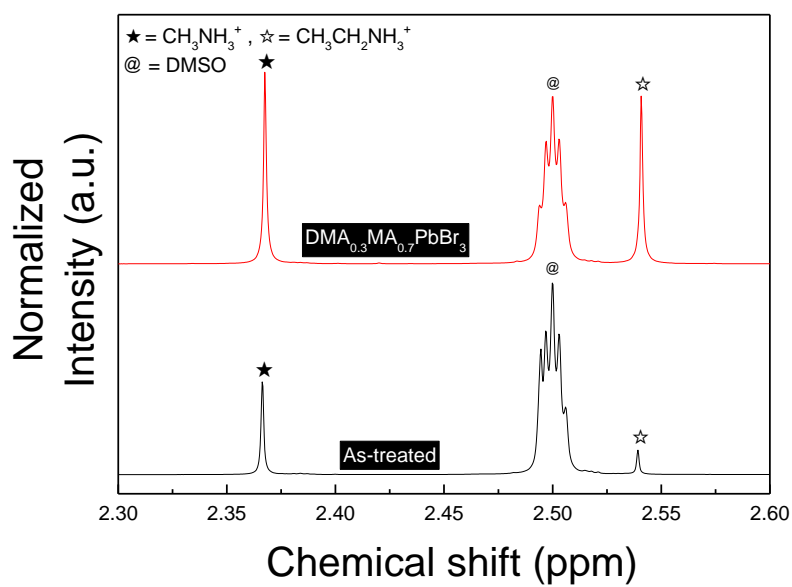


**Figure 4.1.4.** NMR spectra of DMA<sub>0.3</sub>MA<sub>0.7</sub>PbBr<sub>3</sub> film and as-treated film

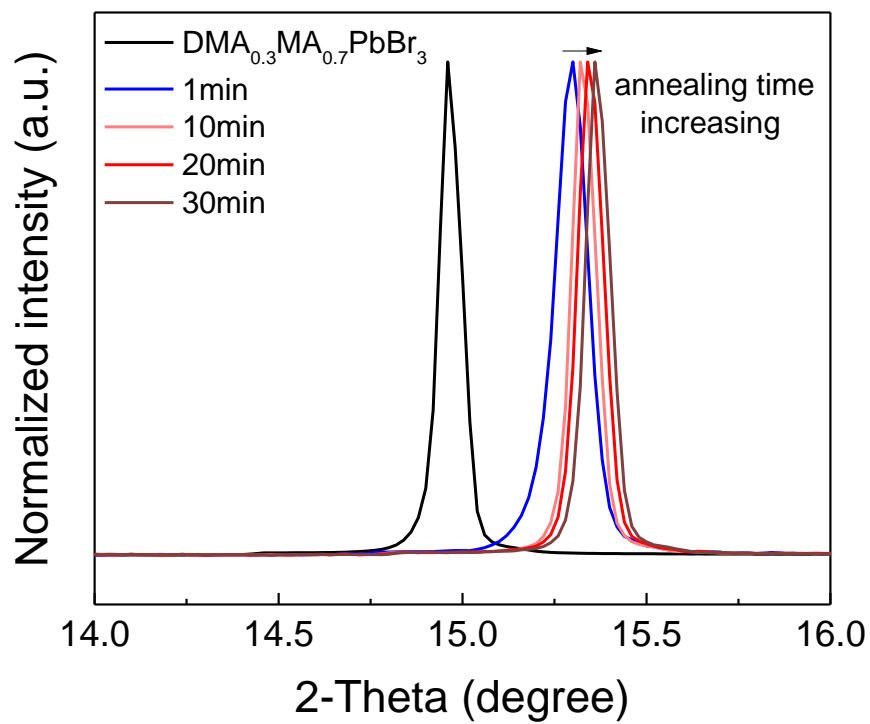


**Figure 4.1.5.** XRD curves of CsPbBr<sub>3</sub> films with increasing annealing time at 225 °C

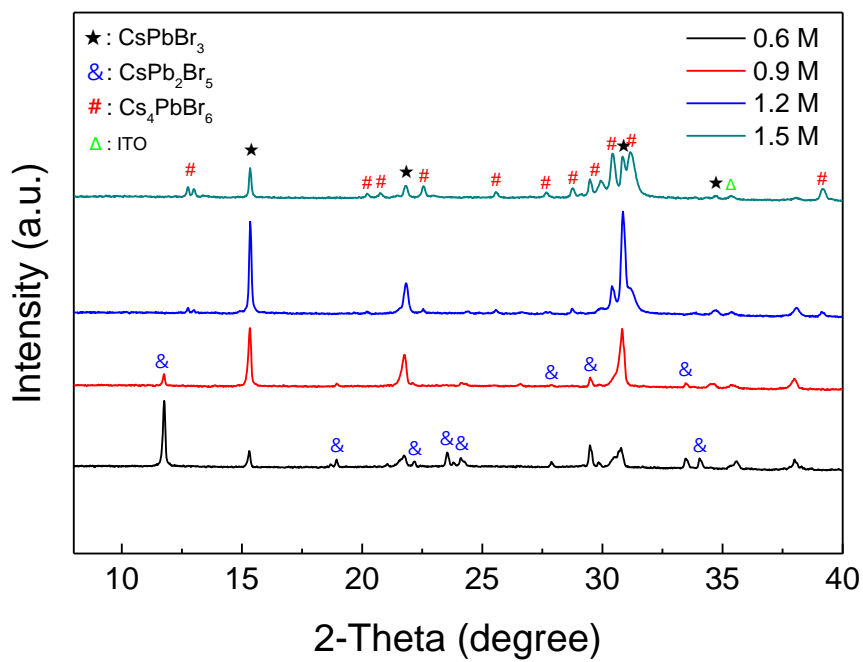


**Figure 4.1.6.** XRD curves of CsPbBr<sub>3</sub> films with increasing concentration of CsAc at 225 °C

RT	Area	Area %	Name	Concentration (µg/m <sup>3</sup> )
9.797	2.53E+09	44	Acetic acid	14919
9.987	9.48E+08	16.46	Guanidine	5583
9.132	7.07E+08	12.28	Isopropylamine	4163
8.837	4.26E+08	7.4	Guanidine	2509
8.627	3.13E+08	5.43	Acetic acid	1841
8.897	1.42E+08	2.46	Ethylamine	834
17.04	1.4E+08	2.44	DMSO	826

**Table 4.1.1.** Mass spectroscopy data which shows type of gas collected at 200 °C

## 4.2 Material analyzation of CsPbBr<sub>3</sub> film

The formation of CsPbBr<sub>3</sub> film through the CsAc treatment mechanism was investigated using various analytical techniques. To confirm the composition of DMA<sub>0.3</sub>MA<sub>0.7</sub>PbBr<sub>3</sub> film and CsPbBr<sub>3</sub> film, We used <sup>1</sup>H NMR spectroscopy. **Fig 4.2.1** shows that the resonance signals for the methylammonium (MA) and dimethylammonium (DMA) cation groups were identified at 2.37 ppm and 2.54 ppm, respectively. The almost complete absence of organic peaks in the post-annealed film(CsPbBr<sub>3</sub>) indicated that both the DMA and MA organic cations were volatilized during the annealing process after CsAc treatment, leading to the well formation of the CsPbBr<sub>3</sub> film.

Also, the validity of this analyzation was confirmed by the agreement between the component ratios determined through measurement and the ratios of DMA and MA used in the experiment. The proton counts derived from the integral of the NMR peaks revealed that the organic film had a composition of 29.8% DMA and 70.2% MA (**Table.4.2.1**). This result corroborated the composition ratio used in the actual experiment, attesting to the reliability and precision of the analytical method employed.

Utilizing X-ray photoelectron spectroscopy (XPS), we obtained supplementary evidence supporting the successful implementation of cation exchange on the post-annealed CsPbBr<sub>3</sub> film. **Fig 4.2.2** shows the N 1s peak of DMA<sub>0.3</sub>MA<sub>0.7</sub>PbBr<sub>3</sub> and CsPbBr<sub>3</sub> film, respectively. N 1s peak represents the -NH<sub>3</sub> bond that constitutes

DMA and MA cation. Disappearance of the N 1s peak at the CsPbBr<sub>3</sub> film indicates that DMA and MA cations were successfully substituted well with Cs cations. Additional xps peaks (Cs 3d, Pb 4f, Br 3d) in **fig 4.2.3** also confirmed the well-presented presence of each element in the CsPbBr<sub>3</sub> film.

To confirm the morphology and thickness of perovskite films before and after CsAc treatment, Scanning Electron Microscopy (SEM) was performed. **Fig.4.2.4** shows the top-view SEM image of DMA<sub>0.3</sub>MA<sub>0.7</sub>PbBr<sub>3</sub> film and CsPbBr<sub>3</sub> film. The morphology of the surface was significantly changed after the CsAc treatment and annealing process. In particular, the formed CsPbBr<sub>3</sub> film has a significant grain size and negligible pinholes. The grain sizes were also measured from the top view images of CsPbBr<sub>3</sub> film by using image J (**Fig.4.2.5**). The size range of the CsPbBr<sub>3</sub> perovskite grain is from 0.8  $\mu\text{m}$  to 4.18  $\mu\text{m}$  with the average of 2.22  $\mu\text{m}$ . Also, the area range of the CsPbBr<sub>3</sub> perovskite grain is from 0.1  $\mu\text{m}^2$  to 11.6  $\mu\text{m}^2$  with the average of 3.55  $\mu\text{m}^2$ .

**Fig.4.2.6** shows the cross-sectional SEM images of DMA<sub>0.3</sub>MA<sub>0.7</sub>PbBr<sub>3</sub> film and CsPbBr<sub>3</sub> film. It can be confirmed that the thickness of CsPbBr<sub>3</sub> film is slightly reduced to 600 nm compared to the DMA<sub>0.3</sub>MA<sub>0.7</sub>PbBr<sub>3</sub> film of 800 nm. It is estimated that the size of perovskite structure was reduced by replacing relatively large DMA cation (272 pm) and MA cation (217 pm) with Cs cation (181 pm)[58]. The thickness of the CsPbBr<sub>3</sub> film is sufficient to be used as a photoactive layer, although it will be further explained later.

**Fig.4.2.7** shows XRD curve of pure CsPbBr<sub>3</sub> film with non-secondary phase. As

mentioned earlier, peaks corresponding to  $15.3^\circ$ ,  $21.7^\circ$ , and  $30.8^\circ$  representing (100), (110), and (200) planes of the  $\text{CsPbBr}_3$  phase were detected. By treating the appropriate concentration of CsAc, it was possible to form a pure  $\text{CsPbBr}_3$  film with little secondary phase.

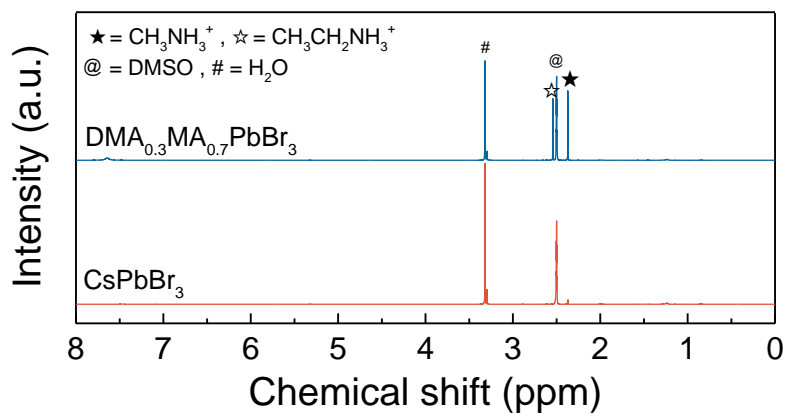


**Figure 4.2.1.** NMR spectra of DMA<sub>0.3</sub>MA<sub>0.7</sub>PbBr<sub>3</sub> film and CsPbBr<sub>3</sub> film



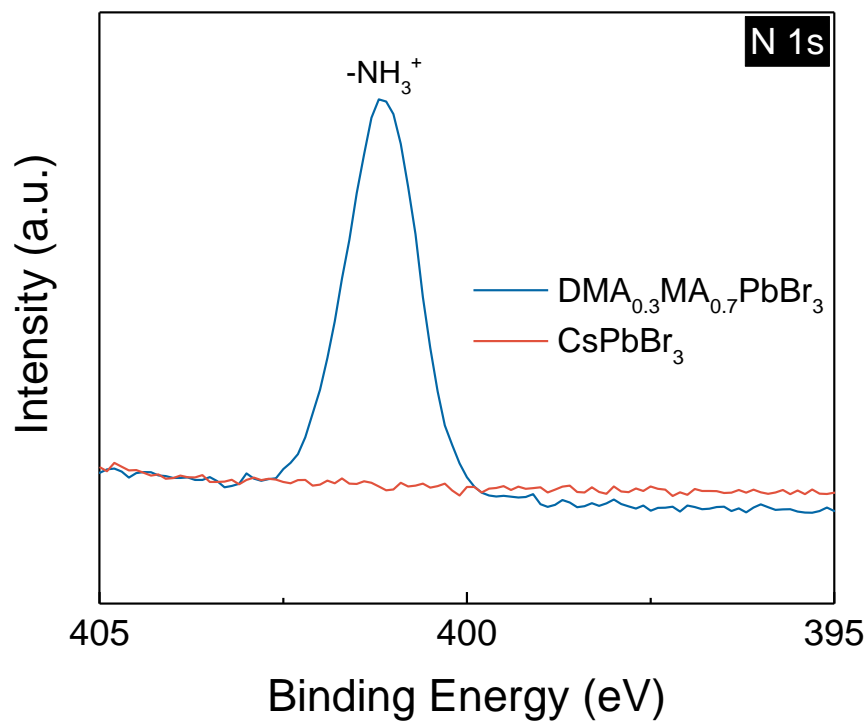


**Figure 4.2.2.** XPS curves (N 1s) of  $\text{DMA}_{0.3}\text{MA}_{0.7}\text{PbBr}_3$  film and  $\text{CsPbBr}_3$  film

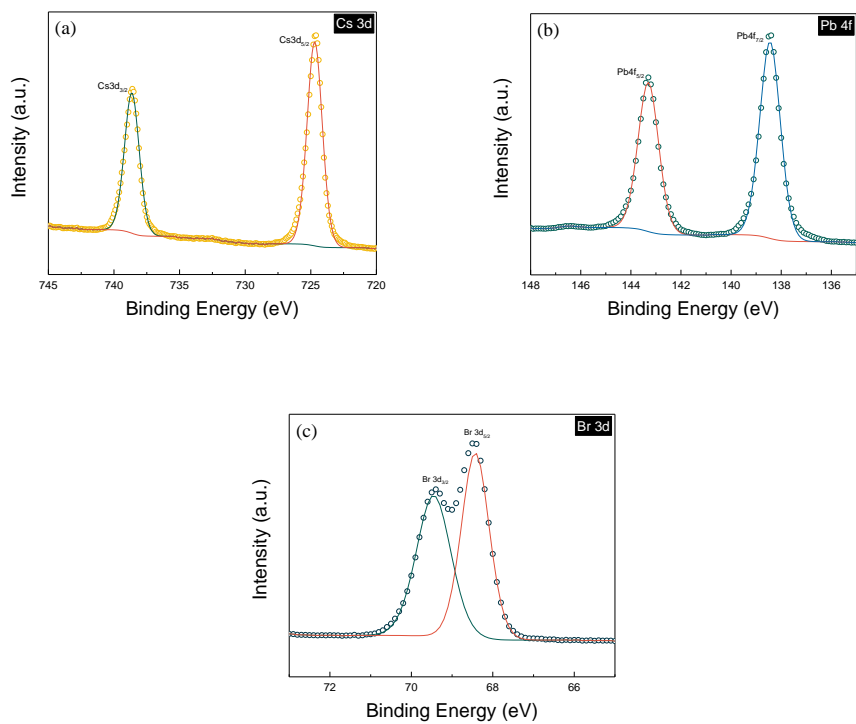


**Figure 4.2.3.** XPS curves ((a) Cs 3d, (b) Pb 4f, (c) Br 3d) of CsPbBr<sub>3</sub> film

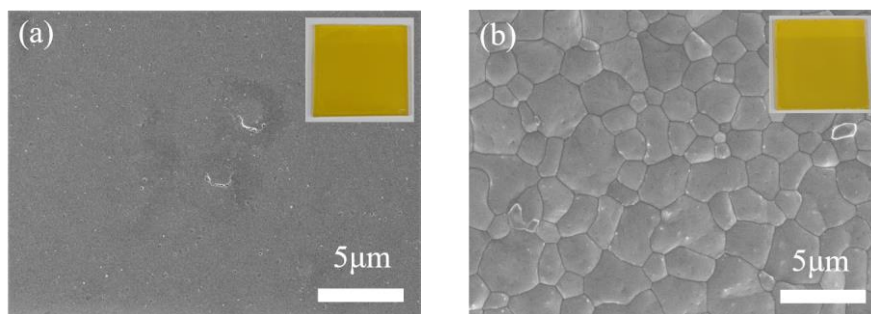


**Figure 4.2.4.** SEM images ((a) top view of DMA<sub>0.3</sub>MA<sub>0.7</sub>PbBr<sub>3</sub> film and (b) CsPbBr<sub>3</sub> film) and photograph of each film

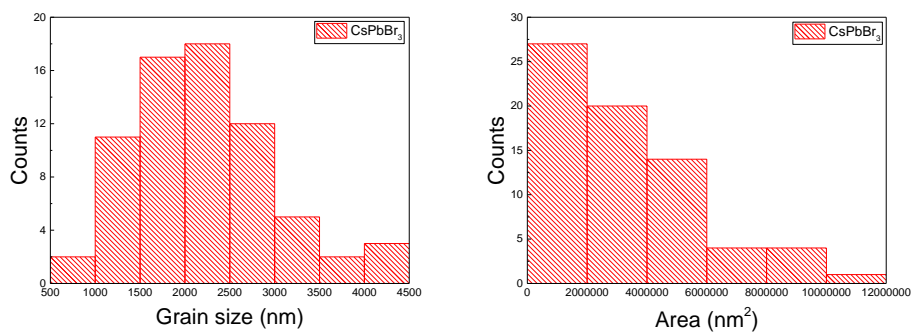


**Figure 4.2.5.** Histograms of the diameters (denoted as grain sizes) and the area of  $\text{CsPbBr}_3$  perovskite grains measured by Image J

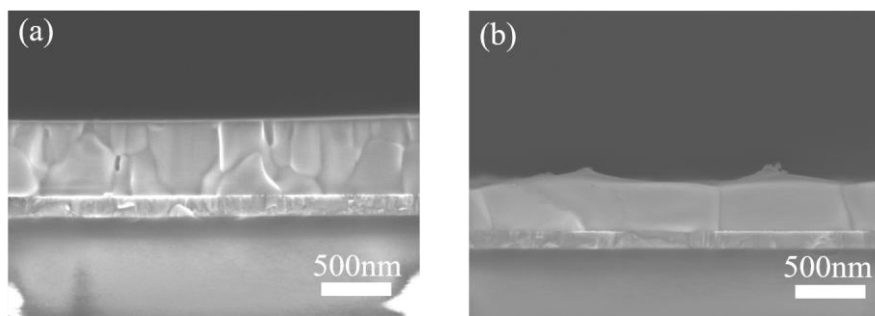


**Figure 4.2.6.** SEM images ((a) cross view of  $\text{DMA}_{0.3}\text{MA}_{0.7}\text{PbBr}_3$  film and (b)  $\text{CsPbBr}_3$  film)

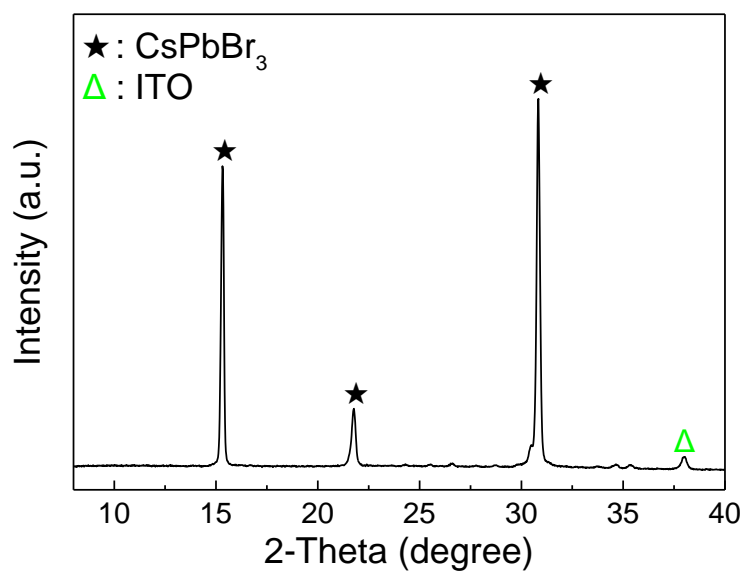


**Figure 4.2.7.** XRD curve of pure CsPbBr<sub>3</sub> film with non-secondary phase

	<b>Peak area (intensity)</b>	<b>Proton #</b>	<b>Area divided by proton #</b>	<b>composition ratio (NMR)</b>
<b>Dimethylammonium cation (DMA<sup>+</sup>)</b>	412077	6	68680	<b>29.80</b>
<b>Methylammonium cation (MA<sup>+</sup>)</b>	485443	3	161814	<b>70.20</b>

**Table 4.2.1.** Calculation of the composition ratio of film through the area of the NMR spectrum corresponding to the MA<sup>+</sup> peak and the DMA<sup>+</sup> peak of the DMA<sub>0.3</sub>MA<sub>0.7</sub>PbBr<sub>3</sub> film

### 4.3 Optical properties of CsPbBr<sub>3</sub> film

We measured the optical properties for the CsPbBr<sub>3</sub> film and built solar cell devices to conduct characterization. **Figure 4.3.1** shows the UV-Vis absorption spectrum of DMA<sub>0.3</sub>MA<sub>0.7</sub>PbBr<sub>3</sub> film and CsPbBr<sub>3</sub>, respectively. It can be seen that the onset of the graph after CsAc treatment starts at a higher wavelength. **Fig.4.3.2** shows relationship between  $(Ah\nu)^2$  and photo energy ( $h\nu$ ). Through Kubelka–Munk equation, it was determined that the optical bandgap of CsPbBr<sub>3</sub> is about 2.36 eV. **Fig.4.3.3** shows photoluminescence (PL) spectrum of the CsPbBr<sub>3</sub>/glass film. An observable emission peak is present at approximately 526 nm, indicating a band gap of roughly 2.36 eV. This measurement aligns with the results obtained from the absorption spectrum analysis.

**Figure 4.3.4** shows the TRPL curves of CsPbBr<sub>3</sub> placed on transport layer. We performed TRPL study to understand the charge-transfer dynamics of CsPbBr<sub>3</sub> over SnO<sub>2</sub> layer and glass layer. The TRPL was measured with the excitation at 526 nm for all samples. The PL decay curves are fitted with bi-exponential function including a fast decay ( $\tau_1$ ) and a slow decay ( $\tau_2$ ) processes [59]. The fast decay component shows how much the quenching of free charge carriers occurs through the transport layer, while the slow decay component is derived from the radiative recombination of free charge carriers. In the CsPbBr<sub>3</sub> film on the glass, a fast decay ( $\tau_1$ ) of 5.98 ns with 45.66 % ratio and a slow decay ( $\tau_2$ ) of 24.351 ns with 54.34 % ratio were measured. On the other hand, in the CsPbBr<sub>3</sub> film on SnO<sub>2</sub>, fast decay ( $\tau_1$ ) of 0.423 ns with 98.74 % ratio and slow decay ( $\tau_2$ ) of 3.466 ns with 1.26 %



ratio were measured (as shown in **Table.4.3.1**). The measured values of both fast decay and slow decay of CsPbBr<sub>3</sub> film on SnO<sub>2</sub> were significantly higher than that of CsPbBr<sub>3</sub> on glass. These observations demonstrate that SnO<sub>2</sub> is an effective transport layer of CsPbBr<sub>3</sub>.

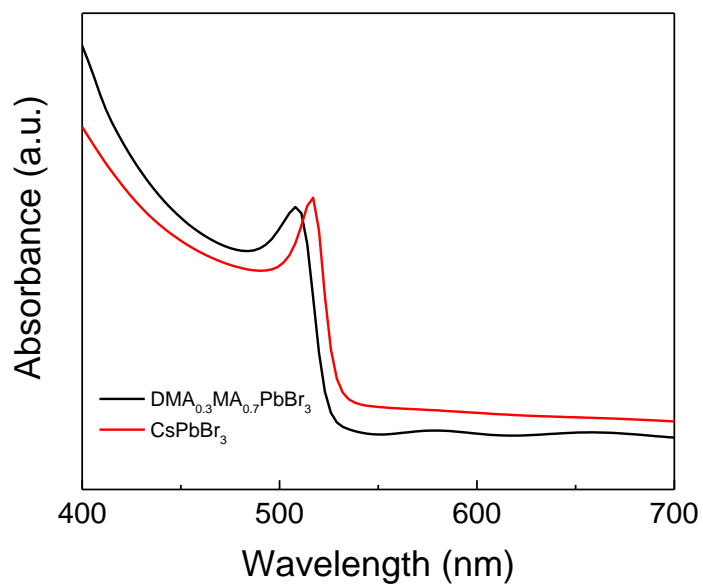


**Figure 4.3.1.** UV-Vis spectra of  $\text{DMA}_{0.3}\text{MA}_{0.7}\text{PbBr}_3$  film and  $\text{CsPbBr}_3$  film

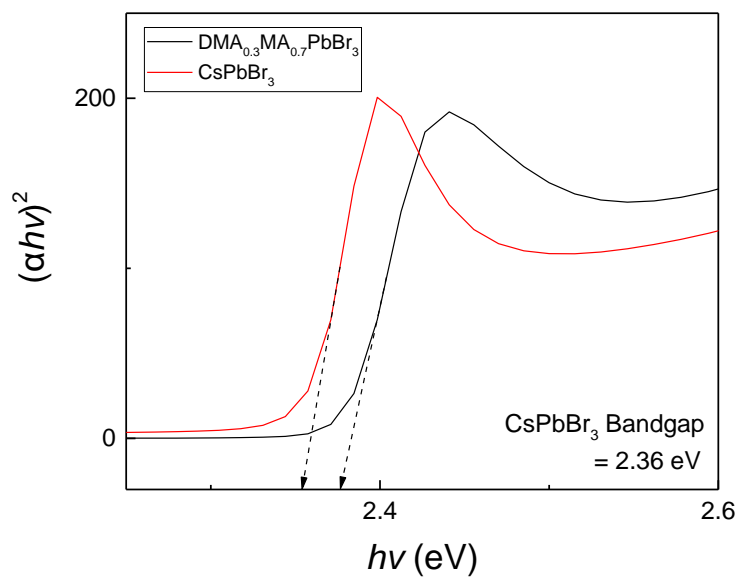


**Figure 4.3.2.** Tauc plot of  $\text{DMA}_{0.3}\text{MA}_{0.7}\text{PbBr}_3$  film and  $\text{CsPbBr}_3$  film from UV-Vis spectra

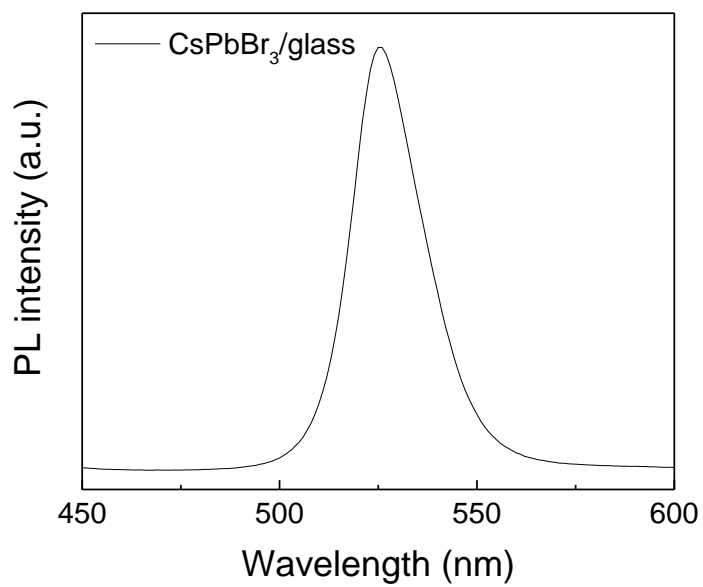


**Figure 4.3.3.** Steady-state PL spectra of CsPbBr<sub>3</sub>/glass film

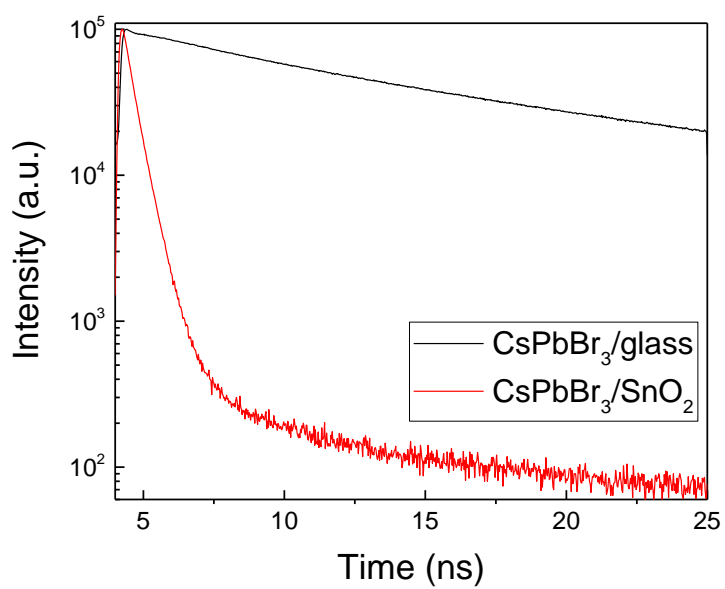


**Figure 4.3.4.** TRPL spectra of CsPbBr<sub>3</sub> film with each layer (glass, SnO<sub>2</sub>)

	$\tau_1$ (ns)	Fraction 1	$\tau_2$ (ns)	Fraction 2
<b>CsPbBr<sub>3</sub>/glass</b>	5.980	45.66 %	24.351	54.34 %
<b>CsPbBr<sub>3</sub>/SnO<sub>2</sub></b>	0.423	98.74 %	3.466	1.26 %

**Table 4.3.1.** Time resolved photoluminescence (TRPL) characterization of the CsPbBr<sub>3</sub> perovskite film on glass and SnO<sub>2</sub> layer

## 4.4 Device characterization

**Figure 4.4.1** shows the light  $J$ - $V$  curves of the best solar cell based on ITO/SnO<sub>2</sub>/CsPbBr<sub>3</sub>/spiro-MeOTAD/Au. Solar cell fabricated through cation exchange strategy shows 5.9% power conversion efficiency (PCE), 1.4V  $V_{oc}$ , 0.66 fill factor (FF), and 6.35mA/cm<sup>2</sup>  $J_{sc}$  under reverse scanning. **Figure 4.4.2** shows incident photon-to-current efficiency (IPCE) spectra of CsPbBr<sub>3</sub> perovskite solar cell. The integrated  $J_{sc}$  obtained through IPCE spectrum was 4.3 mA/cm<sup>2</sup>, which was lower than the  $J_{sc}$  obtained through reverse scan. This phenomenon is also observed in other previously reported CsPbBr<sub>3</sub> solar cells.[22, 60] The difference of  $J_{sc}$  value is presumed to have been caused by the loss of ultraviolet spectra below 350 nm in EQE analysis or by surface defects in the SnO<sub>2</sub> layer.[60, 61]

**Table 4.4.1** shows the stability data of the PSC after storing in N<sub>2</sub> atmosphere (with a temperature of  $\sim 25$  °C) over 120 days without any encapsulation. After storing, the PSC shows 4.5% power conversion efficiency (PCE), 1.13 V  $V_{oc}$ , 0.763 fill factor (FF), and 5.21 mA/cm<sup>2</sup>  $J_{sc}$  under reverse scanning. Although the value of  $V_{oc}$  was reduced compared to before, it was able to maintain more than 80% of the initial efficiency. It is believed that this can be further developed through additional device improvements.

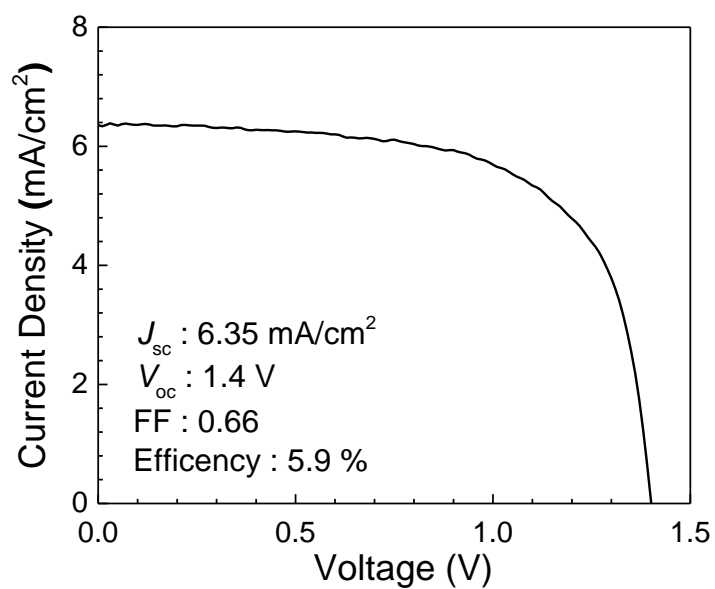


**Figure 4.4.1.** *J*-*V* curve of CsPbBr<sub>3</sub> perovskite solar cell and photovoltaic parameters



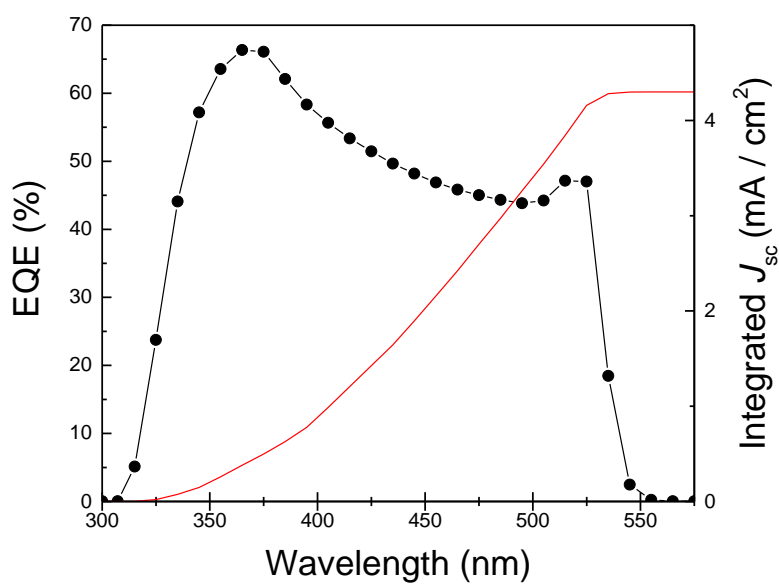


**Figure 4.4.2.** EQE analysis of CsPbBr<sub>3</sub> perovskite solar cell

	$J_{sc}$ (mA/cm <sup>2</sup> )	$V_{oc}$ (V)	Efficiency (%)	FF
<b>Initial</b>	5.39	1.29	5.44	0.783
<b>Over 120days</b>	5.21	1.13	4.50	0.763

**Table 4.4.1.** Stability data of the PSC after storing in N<sub>2</sub> atmosphere (with a temperature of  $\sim 25$  °C) over 120 days without any encapsulation

## Chapter 5. Conclusion

A process for the fabrication of CsPbBr<sub>3</sub> film through the implementation of a cation exchange strategy was first developed. Mechanistic insights into the formation of CsPbBr<sub>3</sub> film were provided through the utilization of X-ray diffraction (XRD), thermogravimetric analysis (TGA), and mass spectroscopy. Confirmation of effective volatilization of organic matter within the resulting CsPbBr<sub>3</sub> film was obtained through nuclear magnetic resonance (NMR) and X-ray photoelectron spectroscopy (XPS). Moreover, scanning electron microscopy (SEM) revealed that the CsPbBr<sub>3</sub> film exhibited an appropriate thickness for its application as a photoactive layer, characterized by a substantial grain size and the absence of voids or pinholes. The determination of CsPbBr<sub>3</sub> film's bandgap was accomplished through photoluminescence (PL) and ultraviolet-visible spectroscopy (UV-Vis), while time-resolved photoluminescence (TRPL) demonstrated the efficient extraction of charges on the SnO<sub>2</sub> electron transport layer by CsPbBr<sub>3</sub>. Finally, the analysis of current-voltage (*I-V*) characteristics and external quantum efficiency (EQE) for CsPbBr<sub>3</sub> solar cell devices shows their significant potential for device fabrication. Collectively, these analyses serve as evidence supporting the suitability of the cation exchange strategy for the formation of CsPbBr<sub>3</sub> solar cell. It is hoped that this strategy will produce devices which have better performance, or be applied to the production of other all-inorganic perovskite solar cells in the future.

## Bibliography

1. *NREL chart*. . Available from: <https://www.nrel.gov/pv/assets/pdfs/best-research-cell-efficiencies.pdf>.
2. Xu, L., et al., *Synthesis of stable and phase-adjustable CsPbBr<sub>3</sub>@Cs<sub>4</sub>PbBr<sub>6</sub> nanocrystals via novel anion–cation reactions*. Nanoscale Advances, 2019. **1**(3): p. 980-988.
3. Li, X., et al., *All-Inorganic CsPbBr<sub>3</sub> Perovskite Solar Cells with 10.45% Efficiency by Evaporation-Assisted Deposition and Setting Intermediate Energy Levels*. ACS Applied Materials & Interfaces, 2019. **11**(33): p. 29746-29752.
4. *Adoption of the Paris Agreement (United Nations, 2015)*. <https://unfccc.int/resource/docs/2015/cop21/eng/l09r01.pdf>. [cited 2015; Available from: <https://unfccc.int/resource/docs/2015/cop21/eng/l09r01.pdf>.
5. Horta, P., et al., *Brazil fosters fossil fuel exploitation despite climate crises and the environmental vulnerabilities*. Marine Policy, 2023. **148**: p. 105423.
6. Perera, F. and K. Nadeau, *Climate change, fossil-fuel pollution, and children's health*. New England Journal of Medicine, 2022. **386**(24): p. 2303-2314.
7. Al-Dainy, G.A., et al., *Hybrid perovskite photovoltaic devices: properties,*

- architecture, and fabrication methods*. Energy Technology, 2017. **5**(3): p. 373-401.
8. Song, Z., et al., *Wide-bandgap, low-bandgap, and tandem perovskite solar cells*. Semiconductor Science and Technology, 2019. **34**(9): p. 093001.
  9. Yang, Z., et al., *Unraveling the exciton binding energy and the dielectric constant in single-crystal methylammonium lead triiodide perovskite*. The journal of physical chemistry letters, 2017. **8**(8): p. 1851-1855.
  10. Oga, H., et al., *Improved understanding of the electronic and energetic landscapes of perovskite solar cells: high local charge carrier mobility, reduced recombination, and extremely shallow traps*. Journal of the American Chemical Society, 2014. **136**(39): p. 13818-13825.
  11. Park, J., et al., *Controlled growth of perovskite layers with volatile alkylammonium chlorides*. Nature, 2023.
  12. Rühle, S., *Tabulated values of the Shockley–Queisser limit for single junction solar cells*. Solar Energy, 2016. **130**: p. 139-147.
  13. Boyd, C.C., et al., *Understanding degradation mechanisms and improving stability of perovskite photovoltaics*. Chemical reviews, 2018. **119**(5): p. 3418-3451.
  14. Wang, D., et al., *Stability of perovskite solar cells*. Solar Energy Materials and Solar Cells, 2016. **147**: p. 255-275.
  15. Noh, M.F.M., et al., *High-humidity processed perovskite solar cells*. Journal of materials chemistry A, 2020. **8**(21): p. 10481-10518.
  16. Dualeh, A., et al., *Thermal behavior of methylammonium lead-trihalide perovskite photovoltaic light harvesters*. Chemistry of Materials, 2014.

- 26**(21): p. 6160-6164.
17. Akbulatov, A.F., et al., *Probing the intrinsic thermal and photochemical stability of hybrid and inorganic lead halide perovskites*. The journal of physical chemistry letters, 2017. **8**(6): p. 1211-1218.
  18. Wang, Y. and H. Sun, *All-inorganic metal halide perovskite nanostructures: from photophysics to light-emitting applications*. Small Methods, 2018. **2**(1): p. 1700252.
  19. Chen, H., et al., *Inorganic Perovskite Solar Cells: A Rapidly Growing Field*. Solar RRL, 2018. **2**(2): p. 1700188.
  20. Marronnier, A., et al., *Anharmonicity and Disorder in the Black Phases of Cesium Lead Iodide Used for Stable Inorganic Perovskite Solar Cells*. ACS Nano, 2018. **12**(4): p. 3477-3486.
  21. Su, Y., et al., *Highly controllable and efficient synthesis of mixed-halide CsPbX<sub>3</sub> (X= Cl, Br, I) perovskite QDs toward the tunability of entire visible light*. ACS applied materials & interfaces, 2017. **9**(38): p. 33020-33028.
  22. Liang, J., et al., *All-inorganic perovskite solar cells*. Journal of the American Chemical Society, 2016. **138**(49): p. 15829-15832.
  23. Duan, J., et al., *High-purity inorganic perovskite films for solar cells with 9.72% efficiency*. Angewandte chemie international edition, 2018. **57**(14): p. 3787-3791.
  24. Liang, J., J. Liu, and Z. Jin, *All-Inorganic Halide Perovskites for Optoelectronics: Progress and Prospects*. Solar Rrl, 2017. **1**(10): p. 1700086.

25. Li, J., et al., *Direct Molecule Substitution Enabled Rapid Transformation of Wet PbBr<sub>2</sub> (DMF) Precursor Films to CsPbBr<sub>3</sub> Perovskite*. ACS Applied Energy Materials, 2021. **4**(7): p. 6414-6421.
26. Teng, P., et al., *Elegant face-down liquid-space-restricted deposition of CsPbBr<sub>3</sub> films for efficient carbon-based all-inorganic planar perovskite solar cells*. ACS applied materials & interfaces, 2018. **10**(11): p. 9541-9546.
27. Ryu, J., et al., *Improving photovoltaic performance of CsPbBr<sub>3</sub> perovskite solar cells by a solvent-assisted rinsing step*. Electrochimica Acta, 2021. **368**: p. 137539.
28. Gao, B. and J. Meng, *High efficiently CsPbBr<sub>3</sub> perovskite solar cells fabricated by multi-step spin coating method*. Solar Energy, 2020. **211**: p. 1223-1229.
29. Yan, J., et al., *Preparation of highly efficient and stable CsPbBr<sub>3</sub> perovskite solar cells based on an anti-solvent rinsing strategy*. Solar Energy Materials and Solar Cells, 2022. **234**: p. 111420.
30. Duan, J., et al., *Spray-assisted deposition of CsPbBr<sub>3</sub> films in ambient air for large-area inorganic perovskite solar cells*. Materials today energy, 2018. **10**: p. 146-152.
31. Ding, X., et al., *Preparation of CsPbBr<sub>3</sub> Films for Efficient Perovskite Solar Cells from Aqueous Solutions*. ACS Applied Energy Materials, 2021. **4**(6): p. 5504-5510.
32. Wang, S., et al., *A green Bi-Solvent system for processing high-quality CsPbBr<sub>3</sub> films in efficient all-inorganic perovskite solar cells*. Materials

Today Physics, 2022. **22**: p. 100614.

33. Liu, C., et al., *Crystallization Kinetics Engineering toward High-Performance and Stable CsPbBr<sub>3</sub>-Based Perovskite Solar Cells*. ACS Applied Energy Materials, 2021. **4**(10): p. 10610-10617.
34. Zhang, C., et al., *Thermal stability of CsPbBr<sub>3</sub> perovskite as revealed by in situ transmission electron microscopy*. APL Materials, 2019. **7**(7): p. 071110.
35. Wang, B. and A. Navrotsky, *Thermodynamics of cesium lead halide (CsPbX<sub>3</sub>, x= I, Br, Cl) perovskites*. Thermochemica Acta, 2021. **695**: p. 178813.
36. Tan, Y., et al., *Ultrastable and Reversible Fluorescent Perovskite Films Used for Flexible Instantaneous Display*. Advanced Functional Materials, 2019. **29**(23): p. 1900730.
37. Stoumpos, C.C., et al., *Crystal growth of the perovskite semiconductor CsPbBr<sub>3</sub>: a new material for high-energy radiation detection*. Crystal growth & design, 2013. **13**(7): p. 2722-2727.
38. Ghaithan, H.M., et al., *Density functional study of cubic, tetragonal, and orthorhombic CsPbBr<sub>3</sub> perovskite*. ACS omega, 2020. **5**(13): p. 7468-7480.
39. Ramasamy, P., et al., *All-inorganic cesium lead halide perovskite nanocrystals for photodetector applications*. Chemical communications, 2016. **52**(10): p. 2067-2070.
40. López, C.A., et al., *Crystal structure features of CsPbBr<sub>3</sub> perovskite prepared by mechanochemical synthesis*. ACS omega, 2020. **5**(11): p. 5931-5938.



41. McMeekin, D.P., et al., *Solution-Processed All-Perovskite Multi-junction Solar Cells*. Joule, 2019. **3**(2): p. 387-401.
42. Wang, P., et al., *Solvent-controlled growth of inorganic perovskite films in dry environment for efficient and stable solar cells*. Nature Communications, 2018. **9**(1): p. 2225.
43. Cao, X., et al., *Water, a green solvent for fabrication of high-quality CsPbBr<sub>3</sub> films for efficient solar cells*. ACS applied materials & interfaces, 2019. **12**(5): p. 5925-5931.
44. Cao, X., et al., *All green solvents for fabrication of CsPbBr<sub>3</sub> films for efficient solar cells guided by the hansen solubility theory*. Solar RRL, 2020. **4**(4): p. 2000008.
45. Jiang, Y., et al., *Reduced-Dimensional  $\alpha$ -CsPbX<sub>3</sub> Perovskites for Efficient and Stable Photovoltaics*. Joule, 2018. **2**(7): p. 1356-1368.
46. Huang, D., et al., *One-step solution deposition of CsPbBr<sub>3</sub> based on precursor engineering for efficient all-inorganic perovskite solar cells*. Journal of Materials Chemistry A, 2019. **7**(39): p. 22420-22428.
47. Akkerman, Q.A., et al., *Nearly monodisperse insulator Cs<sub>4</sub>PbX<sub>6</sub> (X= Cl, Br, I) nanocrystals, their mixed halide compositions, and their transformation into CsPbX<sub>3</sub> nanocrystals*. Nano letters, 2017. **17**(3): p. 1924-1930.
48. Dursun, I., et al., *CsPb<sub>2</sub>Br<sub>5</sub> single crystals: synthesis and characterization*. ChemSusChem, 2017. **10**(19): p. 3746-3749.
49. Li, G., et al., *Shape and phase evolution from CsPbBr<sub>3</sub> perovskite nanocubes to tetragonal CsPb<sub>2</sub>Br<sub>5</sub> nanosheets with an indirect bandgap*.

- Chemical Communications, 2016. **52**(75): p. 11296-11299.
50. Yang, H., et al., *Room-temperature engineering of all-inorganic perovskite nanocrystals with different dimensionalities*. Chemistry of Materials, 2017. **29**(21): p. 8978-8982.
  51. Zhu, J., et al., *Phase Control of Cs-Pb-Br Derivatives to Suppress 0D Cs<sub>4</sub>PbBr<sub>6</sub> for High-Efficiency and Stable All-Inorganic CsPbBr<sub>3</sub> Perovskite Solar Cells*. Small, 2022. **18**(8): p. 2106323.
  52. Meng, Q., et al., *Simultaneous Optimization of Phase and Morphology of CsPbBr<sub>3</sub> Films via Controllable Ostwald Ripening by Ethylene Glycol Monomethylether/Isopropanol Bi-Solvent Engineering*. Advanced Engineering Materials, 2020. **22**(8): p. 2000162.
  53. Zhu, W., et al., *Intermediate phase halide exchange strategy toward a high-quality, thick CsPbBr<sub>3</sub> film for optoelectronic applications*. ACS applied materials & interfaces, 2019. **11**(25): p. 22543-22549.
  54. Xu, J., et al., *Perovskite–fullerene hybrid materials suppress hysteresis in planar diodes*. Nature communications, 2015. **6**(1): p. 7081.
  55. Tsiba Matondo, J., et al., *Lead acetate (PbAc<sub>2</sub>)-derived and chloride-doped MAPbI<sub>3</sub> solar cells with high fill factor resulting from optimized charge transport and trap state properties*. Solar Energy, 2021. **228**: p. 129-139.
  56. Zhang, P., et al., *The disappearing additive: introducing volatile ethyl acetate into a perovskite precursor for fabricating high efficiency stable devices in open air*. Nanoscale, 2022. **14**(13): p. 5204-5213.
  57. Dobbs, W., L. Douce, and B. Heinrich, *1-(4-Alkyloxybenzyl)-3-methyl-1H-*

- imidazol-3-ium organic backbone: A versatile smectogenic moiety.* Beilstein journal of organic chemistry, 2009. **5**(1): p. 62.
58. Kieslich, G., S. Sun, and A.K. Cheetham, *An extended tolerance factor approach for organic–inorganic perovskites.* Chemical science, 2015. **6**(6): p. 3430-3433.
59. Péan, E.V., et al., *Interpreting time-resolved photoluminescence of perovskite materials.* Physical Chemistry Chemical Physics, 2020. **22**(48): p. 28345-28358.
60. Li, H., et al., *Interface engineering using a perovskite derivative phase for efficient and stable CsPbBr<sub>3</sub> solar cells.* Journal of materials chemistry A, 2018. **6**(29): p. 14255-14261.
61. Li, L., et al., *The additive coordination effect on hybrids perovskite crystallization and high-performance solar cell.* Advanced materials, 2016. **28**(44): p. 9862-9868.

## Abstract in Korean

### 국문 초록

전무기  $\text{CsPbBr}_3$  페로브스카이트 태양전지는 유-무기 페로브스카이트 태양전지에 비해 높은 전압 출력을 가지며 습도 및 온도에 대한 높은 안정성으로 주목받고 있다. 그러나,  $\text{CsBr}$ 의 제한된 용해도는 페로브스카이트 태양 전지에 사용하기 위한  $\text{CsPbBr}_3$  박막 생산에 장애물로 남아 있다. 본 연구에서는 전 무기  $\text{CsPbBr}_3$  박막의 합성을 위한 양이온 교환 전략을 제시한다. 우리는 메탄올에 대한  $\text{CsAc}$  (cesium acetate)의 높은 용해도와 two-step spin coating을 이용해 유기  $\text{DMA}_{0.3}\text{MA}_{0.7}\text{PbBr}_3$  박막 ( $\text{DMA} = \text{Dimethylammonium cation}$ ,  $\text{MA} = \text{Methylammonium cation}$ )을 전무기  $\text{CsPbBr}_3$  박막으로 전환했다. 따라서, 균일하고 평평하며 상당한 크기의 결정립과 최소한의 2차 상을 가지는 고품질의  $\text{CsPbBr}_3$  박막이 성공적으로 제조되었다. 또한  $\text{CsPbBr}_3$  박막의 재료적 특성과 광학적 특성, 형성 mechanism에 대해서도 분석되었다. 마지막으로  $\text{CsPbBr}_3$  필름을 이용해 페로브스카이트 태양전지를 구현했으며 이는 현저하게 높은  $V_{oc}$  (1.4 V)와 5.9 %에 달하는 광전 효율을 보여준다.

**주요어:** 세슘레드브로마이드, 용해도, 태양전지, 페로브스카이트, 2단계  
제작법, 세슘 아세테이트

**학번:** 2021-27260